Adjustments for Wind-Induced Undercatch in Snowfall Measurements Based on Precipitation Intensity

MATTEO COLLI,[a] MATTIA STAGNARO, AND LUCA G. LANZA

Department of Civil, Chemical and Environmental Engineering, University of Genoa, and WMO/CIMO Lead Centre "B. Castelli" on Precipitation Intensity, Genoa, Italy

ROY RASMUSSEN

Research Applications Laboratory, National Center for Atmospheric Research, Boulder, Colorado

JULIE M. THÉRIAULT

Department of Earth and Atmospheric Sciences, Centre ESCER, Université du Québec à Montréal, Montreal, Quebec, Canada

(Manuscript received 7 October 2019, in final form 17 February 2020)

ABSTRACT

Adjustments for the wind-induced undercatch of snowfall measurements use transfer functions to account for the expected reduction of the collection efficiency with increasing the wind speed for a particular catching-type gauge. Based on field experiments or numerical simulation, collection efficiency curves as a function of wind speed also involve further explanatory variables such as surface air temperature and/or precipitation type. However, while the wind speed or wind speed and temperature approach is generally effective at reducing the measurement bias, it does not significantly reduce the root-mean-square error (RMSE) of the residuals, implying that part of the variance is still unexplained. In this study, we show that using precipitation intensity as the explanatory variable significantly reduces the scatter of the residuals. This is achieved by optimized curve fitting of field measurements from the Marshall Field Site (Colorado, United States), using a nongradient optimization algorithm to ensure optimal binning of experimental data. The analysis of a recent quality-controlled dataset from the Solid Precipitation Intercomparison Experiment (SPICE) campaign of the World Meteorological Organization confirms the scatter reduction, showing that this approach is suitable to a variety of locations and catching-type gauges. Using computational fluid dynamics simulations, we demonstrate that the physical basis of the reduction in RMSE is the correlation of precipitation intensity with the particle size distribution. Overall, these findings could be relevant in operational conditions since the proposed adjustment of precipitation measurements only requires wind sensor and precipitation gauge data.

1. Introduction

In situ liquid and solid automatic precipitation measurements commonly employ catching-type gauges to collect hydrometeors as they approach the surface. Factors affecting the capability of the gauge to collect and measure the actual precipitation occurring at a given site include wind, wetting, splashing, etc. (WMO 2014). For a given gauge, we define the collection efficiency (CE) as the ratio between the precipitation amount P_{meas} (mm) measured by the gauge and the true precipitation P_{true} (mm):

$$\text{CE} = \frac{P_{\text{meas}}}{P_{\text{true}}}. \tag{1}$$

The true precipitation is generally unknown. When CE is evaluated from analytical or numerical calculations P_{true} is given as an input, while in field studies it is

Supplemental information related to this paper is available at the Journals Online website: https://doi.org/10.1175/JHM-D-19-0222.s1.

[a] Current affiliation: Artys S.r.l., Genoa, Italy.

Corresponding author: Mattia Stagnaro, mattia.stagnaro@unige.it

DOI: 10.1175/JHM-D-19-0222.1

common to replace P_{true} with a reference value P_{ref} obtained from high-quality instruments and/or specific installations.

In case of snowfall measurements, wind plays a dominant role in reducing the gauge collection efficiency (Goodison et al. 1998; Rasmussen et al. 2012). Nešpor and Sevruk (1999) and Constantinescu et al. (2007) used computational fluid dynamics (CFD) simulations to evaluate the wind-induced undercatch of rainfall. Thériault et al. (2012) used it for snowfall and compared the results with detailed observations of snow crystals. A recent analysis by Colli et al. (2015) showed good agreement between the collection efficiency predicted by time averaged models of wind speed and particle trajectories and the field observations made at the NCAR–NOAA–FAA Marshall Field Site (Colorado, United States; Rasmussen et al. 2012). A shielded automatic gauge in the Double Fence Automatic Reference (DFAR) configuration provided the reference precipitation, since this reference system was designated within Solid Precipitation Intercomparison Experiment (SPICE) as the international standard gauge/shield configuration for snowfall measurement (Nitu et al. 2018).

Adjustment methodologies (e.g., Yang et al. 1999) have been developed and are typically algebraic relationships between CE and the mean wind speed U_w ($m\,s^{-1}$) at the gauge catchment height, also referred to as transfer functions. Thériault et al. (2012) and Colli et al. (2015) specified CE curves as a function of wind speed for different solid precipitation types (following Rasmussen et al. 1999) and particle size distributions (PSD). Wolff et al. (2015) proposed a sigmoidal function for the CE using the observations collected in Haukeliseter (Norway). This relationship includes the air temperature as an additional parameter to consider the likely amount of water contained in the precipitation particles.

Wolff et al. (2015) and Colli et al. (2016b) showed that the influence of the type of precipitation on the catch performance of precipitation gauges could be considered by specifying the CE values according to the air temperature when considering the transition from snow to rain. The air temperature (T) is an efficient indicator to determine the type of precipitation (Sims and Liu 2015) such as rainfall ($T > 2$°C), wet snow ($-2° < T < +2$°C) and dry snow ($T < -2$°C). However, this is not representative of the large variety of crystal types and the degree of riming (Rasmussen et al. 1999; Thériault et al. 2012).

Recently, Kochendorfer et al. (2017a,b) described a simplified inverse exponential formulation for the universal transfer function using wind speed and air temperature. Their analysis is based on measurements collected at the Marshall and Haukeliseter field sites (Kochendorfer et al. 2017a) and at eight SPICE field sites (Kochendorfer et al. (2017b) and highlighted that a significant root-mean-square error (RMSE) still remain even though a transfer function can reduce the gauge's bias to near zero. Thériault et al. (2012), using observations and simulations, suggest that the RMSE is due to the large variability in the particle type and size distribution of snowfall. The temperature can help determining the phase of the precipitation but not the size of hydrometeors, which helps explain the small impact of air temperature on the RMSE. Recent CFD studies showed that the snowfall measurements performed by the DFAR can also be affected by a significant bias in windy conditions, with residual uncertainties related to the microphysical characteristics of precipitation (Thériault et al. 2015).

Further numerical simulations were conducted to study the fundamental processes leading to the large scatter in the data for a given wind speed. Colli et al. (2015) presented dry snow CE estimations for an unshielded and a Single Alter (SA) shielded gauges (Alter 1937) based on data from the Marshall Field Site. The comparison of CFD simulations with the observations (Thériault et al. 2012; Colli et al. 2015) showed that a large part of the CE variability for a given wind speed is explained by the particle size distribution. Thériault et al. (2012, 2015) reported that the catch performance of a shielded gauge is also related to the particle's fall speed in the vicinity of the gauge.

These studies suggest that the particle type, size, and the wind field can affect the gauge collection efficiency. To explore this further, we note that it is possible to represent the size distribution of precipitation particles by an inverse exponential function (Marshall and Palmer 1948) that depends on two parameters, the slope and the intercept of its logarithmic representation. Pruppacher and Klett (2010) show that the slope of the PSD is closely related to the precipitation rate. As the precipitation rate increases, the slope of the size distribution decreases, leading to a higher concentration of large particles. Previous studies (e.g., Folland 1988; Nešpor and Sevruk 1999), focusing on liquid precipitation only, specified the functional relationships between wind-induced undercatch and wind for different rainfall rate classes. Therefore, we suggest that the precipitation rate, that is, snowfall intensity (SI), can be used to improve adjustments based on the CE curves. Such a possibility is explored in this paper and is shown to significantly reduce the RMSE.

Our method of investigation first considers precipitation gauge data collected at the Marshall (Colorado, United States), CARE (Canada), and Haukeliseter (Norway) field test sites. Second, using CFD simulations, different PSDs are numerically tested and the CE

is evaluated based on the associated precipitation intensity. This allows testing the proposed hypothesis in a simplified environment where the noise that is typical of experimental datasets is avoided. The results show a good agreement of the CE values with field data and a clear dependency on the SI.

The measurements and the data processing method used to perform the field data analysis are presented in section 2. Section 3 reports on the observed correlation between CE and the measured SI or the environmental temperature. A description of the data binning optimization according to SI is also included. The influence of the chosen temporal aggregation of measurements on the derived CE is described in section 4. In section 5, the dependency between the CE and the measured SI is investigated using CFD simulations with the aim of providing a physical basis for the correlation observed in section 3.

2. Methodology of field data analysis

a. Field data processing

The development and testing of new methodologies to retrieve the CE requires the availability of quality controlled, high-frequency meteorological measurements from a properly instrumented testbed. The snowfall measurements used in this study were collected by two weighing gauge systems, one consisting of an SA shield surrounding a Geonor T200B weighing gauge with a 6-s sampling frequency and the second a DFIR shielded Geonor T200B. Both systems were collocated at the Marshall Field Site (Rasmussen et al. 2012) during 2013–15 as part of the SPICE program by WMO (Nitu et al. 2018). Ancillary data were also collected at the Marshall Field Site every minute to support investigation into factors that might affect the CE. The SA Geonor T200B gauge measurements are compared to those made by the DFIR shielded Geonor T200B gauge, which was defined as the working automated reference for WMO-SPICE (Kochendorfer et al. 2018).

Wind speed is measured 2 m above the ground surface using a propeller anemometer (Model 05103 Wind Monitor, RM Young) whereas the temperature was measured 1.5 m above the ground surface using a fan-aspirated (Model 076B Radiation Shield, Met One Instruments) platinum resistance thermometer (Model CS500-L, Campbell Scientific).

Geonor weighing gauges are based on vibrating wire technology. Noise in the output is typically due to environmental factors that cause oscillations of the measuring bucket. These effects have been reduced by postprocessing the 6 s raw time series with a Gaussian linear time-invariant filter characterized by a filtering window equal to 2 min and a standard deviation equal to 1 min. A correction of the vibrating wires' sensitivity to the environmental temperature has been applied as well. In addition, an automatic quality control was performed to check the occurrence of missing data, decreasing trends or jumps in the precipitation time series, and inconsistent data from the three vibrating wires of the Geonor T200B gauge (Reverdin 2016).

The measured CE, already defined in section 1, is now better specified as the ratio between the precipitation amount measured by the SA shielded gauge (P_{SA}) and the one measured by the DFIR shielded gauge (P_{DFIR}), as follows:

$$\mathrm{CE} = \frac{P_{SA}}{P_{DFIR}}. \tag{2}$$

As for the Marshall Field Site, we focused on the WMO-SPICE 30-min quality controlled site event datasets (SEDS; see online supplemental material), according to the procedure described in Reverdin (2016) and Kochendorfer et al. (2017b). Only 30-min data with reference precipitation (P_{DFIR}) larger or equal to 0.25 mm were considered, for a total of 72 days of precipitation recorded from October 2013 to April 2015. The dataset was further reduced to consider events with an environmental temperature less than −2°C, to avoid the occurrence of liquid precipitation (Colli et al. 2015), resulting in a final dataset of 213 thirty-minute intervals (A-SEDS in Table 1).

The SEDSs from CARE (Canada) and Haukeliseter (Norway) were processed in a similar way and denoted B-SEDS and C-SEDS respectively in Table 1. At the CARE field site, the wind speed and temperature measured at 2 m above ground were measured by a NWS425 anemometer and HMP155 thermometer (Vaisala). At the Haukeliseter field site, wind speed measurements were made at 10 m level above the ground by a WindObserver II anemometer manufactured by Gill Instruments and a PT100 platinum resistance thermometer sensor measured the environmental temperature. We adopted the Kochendorfer et al. (2017a) approach to converting 10-m wind to 2-m gauge height wind. This entails correcting the 10-m wind by a factor of 0.71; $U_{10m} \times 0.71$, assuming a logarithmic vertical profile of wind speed (Thom 1975).

Because the snowfall type, particle size distribution and terminal velocity at a given location are highly variable in time, shorter time intervals were also tested. Most meteorological services (Matrosov et al. 2009; Gergely and Garrett 2016) use 30- or 60-min intervals. To investigate the influence of the sampling interval on the CE variation with wind speed, the original 1-min dataset from the Marshall Field Site from January 2013

TABLE 1. Location, measurement period, time interval, and data consistency of SEDS (site event dataset) considered in the analysis.

Dataset	Location	Period	Time interval (min)	No. of data
A	Marshall (United States)	Jan 2013–Apr 2015	1	6943
A-SEDS	Marshall (United States)	Oct 2013–Apr 2015	30	213
B-SEDS	CARE (Canada)	Nov 2013–Apr 2015	30	234
C-SEDS	Haukeliseter (Norway)	Nov 2013–Apr 2015	30	485

to April 2015 was aggregated to 5-, 10-, and 20-min time intervals. The wind speed and temperature datasets were averaged over the same time intervals. A minimum snowfall rate was set for the DFAR as $SI_{DFIR} = 0.5\,mm\,h^{-1}$ to avoid cases of very light snow. Under these conditions, the total dataset—indicated as A in Table 1—is composed of a total of 6943 one-minute samples recorded during 29 different precipitation events.

b. *Data analysis method*

We analyze the CE as a function of wind speed and air temperature, as suggested by Wolff et al. (2015) and Kochendorfer et al. (2017a), then we investigate the role of SI as an alternative explanatory variable. The SI is linked to the PSD and the vertical velocity of particles by the following equation:

$$SI = \alpha \int_{D_{min}}^{D_{max}} N(D) \times w_p(D) \times D^3\, dD, \qquad (3)$$

where D is the particle diameter (mm), $N(D)$ the number of particles with diameter D, $w_p(D)$ the vertical velocity ($m\,s^{-1}$), and α is a factor that accounts for the shape of the snowflakes.

The CE function suggested by Kochendorfer et al. (2017a) as a function of wind and the air temperature is expressed as

$$CE = e^{-a(U_w)(1-\{\tan^{-1}[b(T)]\})}, \qquad (4)$$

where $a(U_w) = a \times U_w$ and $b(T) = b \times T$, U_w is wind velocity, T is the air temperature, while a, b, and c are empirical coefficients that depend on the gauge, shield, and site (Tables 2 and 3 of Kochendorfer et al. 2017a).

The role of the SI is tested here by simply assuming that SI rather than T actually shapes the collection efficiency, therefore adopting the following equation:

$$CE = e^{-a \times U_w \{1-[\tan^{-1}(b \times SI)+c]\}}, \qquad (5)$$

where a, b, and c are numerical best-fit coefficients. Equation (4) considers the precipitation phase as a driving factor, while in Eq. (5) the size distribution of the hydrometeors is considered.

3. Results from the field data analysis

The empirical CE for the SA shielded gauge as a function of wind speed is shown in Fig. 1 using the 30-min dataset A-SEDS. In the two panels, CE data are color coded according to the air temperature T (Fig. 1a) and to the snowfall intensity SI_{SA} (Fig. 1b). No significant correlation is visually evident in Fig. 1a, while Fig. 1b shows a distinct cluster of low precipitation rates in the lower part of the CE range. Although for any given wind speed different CE may occur depending on the SI_{SA}, there is a higher CE observed when the gauge collects the higher SI. This trend becomes more evident when the mean horizontal wind speed is higher than $2\,m\,s^{-1}$.

One explanation of the larger CE is related to larger particle sizes having trajectories that are less prone to deflection by the deformed airflow above the gauge collector [as detailed in Thériault et al. (2012) for different crystal types and by Colli et al. (2016a,b)]. Colli et al. (2015) showed a correlation between the slope parameter of the PSD outside the tested gauge and its

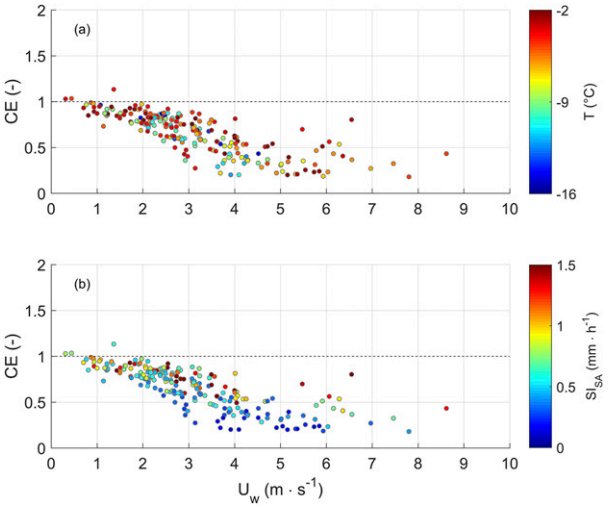

FIG. 1. Collection efficiency $CE = P_{SA}/P_{DFIR}$ for the 30 min SA shielded gauge measurements from the Marshall Field Site in the period October 2013–April 2015. Data are color coded according to (a) the air temperature T and (b) the measured snowfall intensity SI_{SA}.

TABLE 2. Best-fit coefficients a, b, and c of the inverse exponential function, number of 30-min intervals used (n), and linear correlation coefficient r based on measurements made by the SA shielded gauge at the Marshall (Colorado, United States), CARE (Canada), and Haukeliseter (Norway) field test sites from October 2013 to April 2015. Coefficients are calculated for both the CE(U_w, SI_{SA}) and CE(U_w, T) at each field test site.

Field test site	CE formulation	a	b	c	n	r
Marshall	CE(U_w, SI_{SA})	0.4156	8.7795	−0.7062	213	0.91
	CE(U_w, T)	0.0560	0.2148	−0.8542	213	0.82
CARE	CE(U_w, SI_{SA})	12.5937	338.0402	−0.5737	234	0.84
	CE(U_w, T)	0.3103	0.0116	0.7711	234	0.7
Haukeliseter	CE(U_w, SI_{SA})	0.5557	11.0022	−0.7073	485	0.87
	CE(U_w, T)	0.1713	0.0767	−0.0579	485	0.75

CE by means of CFD analysis and the results were supported by disdrometers field data. Larger particles are associated with lower slope of the PSD and therefore higher SI (Pruppacher and Klett 2010).

A least squares regression was performed on the inverse exponential function of the CE based on wind speed and temperature, Eq. (4), and the one based on wind speed and SI, Eq. (5). The coefficients obtained from the best-fit analysis are listed in Table 2.

The two regressions are presented in Fig. 2. These are the CE(U_w, T) (Fig. 2a) and CE(U_w, SI_{SA}) (Fig. 2b) surfaces together with the field measurements (red dots). The CE surfaces are color coded. The CE(U_w, SI_{SA}) regression shows a relevant dependency on the measured snowfall intensity. In contrast, the CE(U_w, T) regression shows a weaker dependency on the environmental temperature T than on the SI.

To ensure optimal regression of the observed dependency between the CE and the SI measured by the uncorrected gauge, a nongradient multiobjective genetic optimization algorithm, implemented in the DAKOTA open source toolkit (Eldred et al. 2007), was used to retrieve the best SI class limits. The following classes were obtained: $0.0 < SI_{SA} \leq 0.4\,mm\,h^{-1}$, $0.4 < SI_{SA} \leq 0.6\,mm\,h^{-1}$, $0.6 < SI_{SA} \leq 1.0\,mm\,h^{-1}$, and $1.0 < SI_{SA} \leq 1.5\,mm\,h^{-1}$. The optimization objectives were to maintain a significant sample size for each bin and to minimize the scatter (RMSE) of the residuals. Figure 3 presents CE(U_w, SI_{SA}) plots for smaller subsets of field data according to the optimized SI classes. The results show that each intensity category has a different fit to a sigmoid function, with the lowest SI class having the steepest decrease in CE with increasing wind speed. This is again explained by the highest intensities being associated with the largest particles, therefore slowly decreasing their CE with wind speed.

Figure 4 compares best-fit CE curves computed as a function of wind speed and either temperature or the SI. It shows that there is evidence of much stronger dependence on the SI classification (solid lines) than on temperature (dotted lines). The four CE(U_w, T) curves (dashed lines) show similar trends and are very close to

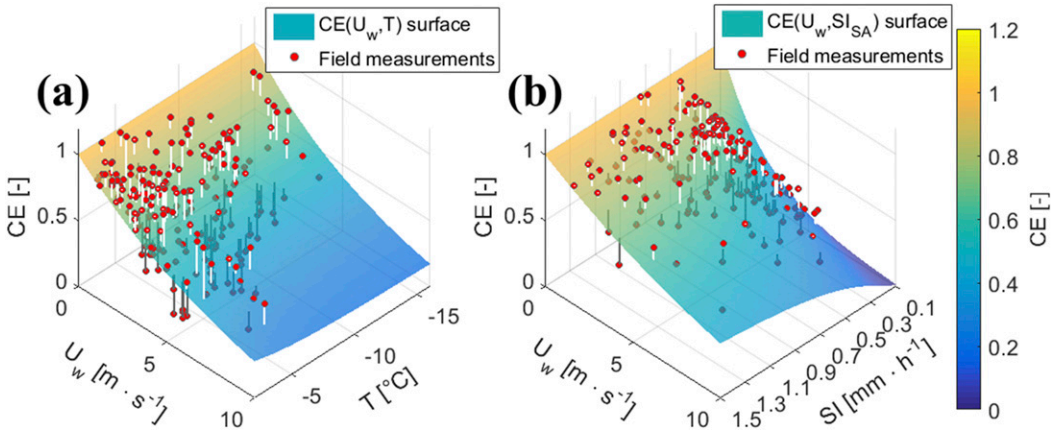

FIG. 2. Best-fit CE surfaces for the 30-min SA shielded snow gauge measurements made at the Marshall Field Site (red dots). Two regressions are shown by expressing CE as a function of the wind speed and either (a) the air temperature T or (b) the measured snowfall intensity SI_{SA}.

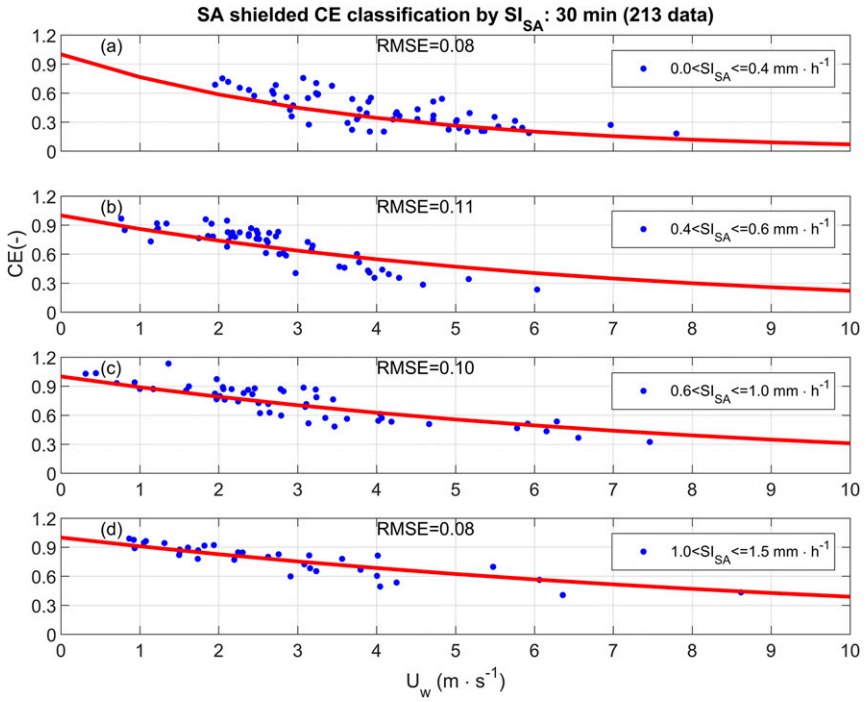

FIG. 3. Empirical CE for the 30-min SA shielded snow gauge measurements made at the Marshall Field Site as a function of wind speed. The solid line in each panel is the sigmoidal best fit to the data. Each panel represents a different SI range as defined in the legends and reports the RMSE of the residuals.

each other, demonstrating that there is no significant correlation of the CE with temperature below −2°C. In contrast, the curves show a distinct separation when categorized by SI for the 30-min dataset (solid lines).

An evaluation of the improved snowfall accumulation estimates when using the SI-dependent curve fit is shown in Fig. 5a, where the corrected CE is shown and the RMSE of the residuals is reported. The residual scatter is quantified by a RMSE equal to 0.10 and the color coded distribution based on the environmental temperature appears quite random. A larger scatter (RMSE = 0.14) is observed when the measurements are corrected using wind speed and temperature (Fig. 5b, traditional approach). Note that Fig. 5b shows a color separated dependence of the residuals on the SI, indicating that notwithstanding the CE(U_w, T) correction some form of dependency persists between the SA shielded gauge undercatch and the characteristics of precipitation.

The best fit coefficients of the collection efficiency regression obtained with the CARE and Haukeliseter datasets are reported in Table 2 for both the CE(U_w, T) and CE(U_w, SI_{SA}) formulations. The correction of the measurements based on such transfer functions is shown in Figs. 6 and 7. The RMSEs of the residuals for the CARE measurements are equal to 0.09 in the case of CE(U_w, SI_{SA}) and 0.12 in the case of CE(U_w, T) while the residuals for the Haukeliseter measurements show RMSEs that are equal to 0.16 and 0.22, respectively. These RMSE results confirm that the approach based on the wind speed and SI leads to an improved correction

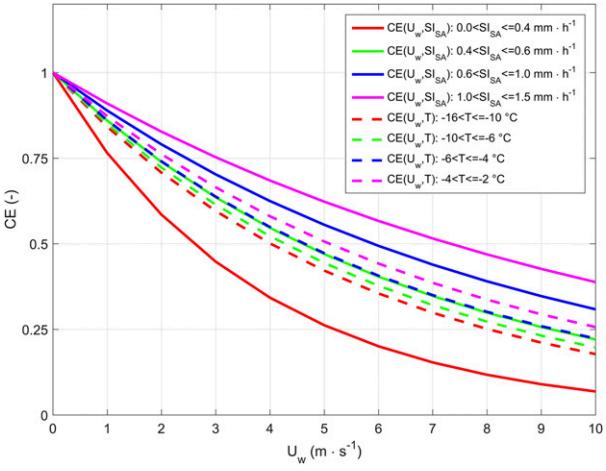

FIG. 4. Best-fit CE curves of the 30-min measurements made by the SA shielded snow gauge at the Marshall Field Site using either the air temperature T (dashed lines) or the measured SI (solid lines). SI curves are the same as in Fig. 3.

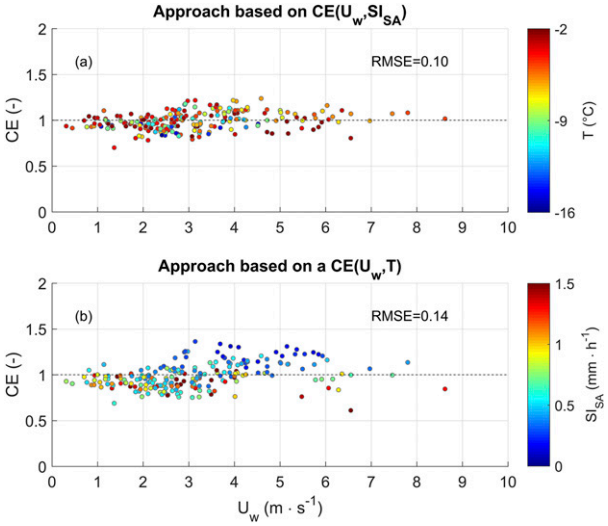

FIG. 5. Residuals obtained after correcting the 30-min snow gauge measurements from the SA shielded at Marshall Field Site using (a) Eq. (5) and (b) Eq. (4), with the associated RMSE values. Residuals are color coded according to (a) the environmental temperature T and (b) the snowfall intensity SI_{SA}.

of the solid precipitation measurements. The results of the field data analysis suggest that the environmental temperature can be used to provide an approximated criterion to recognize the precipitation phase (liquid, mixed, or solid) while the SI is a more efficient explanatory variable since it is directly related to the PSD.

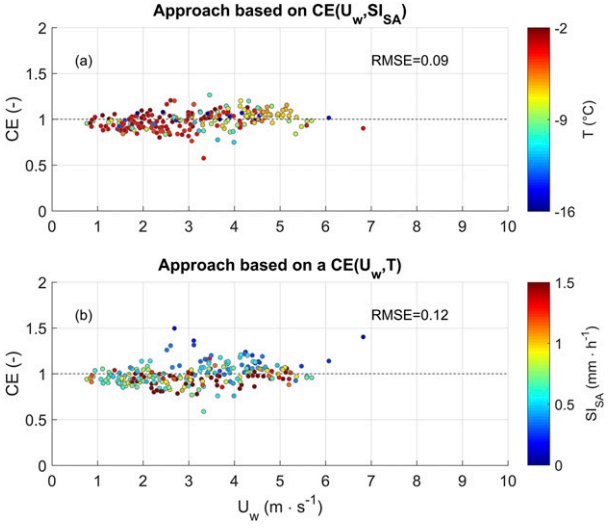

FIG. 6. Residuals obtained after correcting the 30-min snow gauge measurements from the SA shielded at CARE (Canada) field test site using (a) Eq. (5) and (b) Eq. (4), with the associated RMSE values. Residuals are color coded according to (a) the environmental temperature T and (b) the snowfall intensity SI_{SA}.

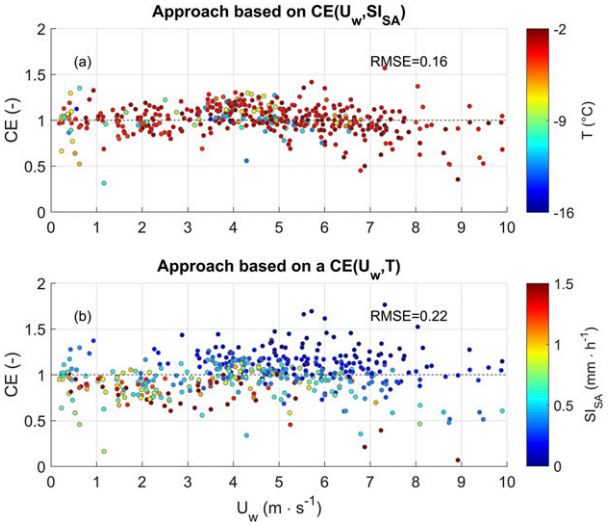

FIG. 7. Residuals obtained after correcting the 30-min snow gauge measurements from the SA shielded at the Haukeliseter (Norway) field test site using (a) Eq. (5) and (b) Eq. (4), with the associated RMSE values. Residuals are color coded according to (a) the environmental temperature T and (b) the snowfall intensity SI_{SA}.

4. Sensitivity to the time aggregation

The analysis of field data proposed in section 3 has been repeated on the 1-min measurements performed by the SA shielded gauge at the Marshall Field Site from January 2013 to April 2015 and aggregated over time intervals equal to 5, 10, 30, and 60 min. The regression coefficients obtained by applying the inverse exponential functions described by Eqs. (2) and (3) are reported in Table 3. Figure 8 shows the CE curves calculated for different measured snowfall intensities SI_{SA} and time resolutions Δt. In all cases, a strong CE dependency on SI_{SA} draws distinct variations with wind speed, which do not overlap with each other. On the other hand, CE curves obtained from observations at a larger aggregation time (e.g., 30 min) tend to be closer to each other, and hence the dependency on SI slightly decreases. This is partially explained by the fact that SI_{SA} is strongly aggregation dependent and when the intensity measurements are averaged over a large time interval they become less representative of the internal variability.

The representativeness of the proposed CE(U_w, T) transfer functions (represented by their linear correlation coefficient r in Table 3) with respect to the field measurements decreases sharply below 5 min for temperature, while it does not for CE(U_w, SI_{SA}), suggesting that the T dependence becomes weaker at high resolution while the SI_{SA} dependence not so much. A similar behavior is reported in Table 4 in terms of RMSE,

TABLE 3. Coefficients (a, b, and c) of the inverse exponential function fitted at various aggregation intervals for the CE(U_w, T) and CE(U_w, SI_{SA}) formulations, with the associated linear correlation coefficient r, and number of data available (n). The calculation used measurements made by the SA shielded gauge at the Marshall Field Site from January 2013 to April 2015.

	CE(U_w, T)				CE(U_w, SI_{SA})				
Δt (min)	A (—)	B (—)	C (—)	r (—)	A (—)	B (—)	C (—)	r (—)	n (—)
1	0.1687	0.3419	0.8915	0.57	21.3664	290.6924	−0.5718	0.86	6943
5	0.1885	0.6830	1.311 14	0.72	234.801	3630.7	−0.5710	0.89	1405
10	0.1281	0.5099	0.8071	0.81	1.3253	26.2030	−0.6198	0.91	697
30	0.1144	0.5177	0.6670	0.87	0.4325	9.2192	−0.7403	0.92	226
60	0.2196	1.2223	1.6033	0.89	0.3078	6.1165	−0.8012	0.94	115

where the transition between the 5-min and the 1-min aggregation intervals yields the larger RMSE increase for the CE(U_w, T) formulation. Therefore, the dependence on SI_{SA} is more robust with respect to time aggregation. As shown in section 3, WMO-SPICE used a 30-min aggregation interval to assess the CE, which still shows significant variability at any given wind speed.

Figure 8 demonstrates that the 10-min time interval may represent a trade-off point between the availability of correlated SI_{SA} and CE observations and the need of aggregating the measurement over a longer interval during low precipitation intensity. An evaluation of the impact of the data integration time on the correction of the P_{SA} observations was made by considering snowfall accumulations computed at different aggregation intervals. Table 4 shows that a larger dispersion of the CE of the corrected measurements (quantified by the RMSE) around the optimal value (CE = 1) is observed when short aggregation intervals are considered. Table 4 also shows that smaller RMSEs are systematically observed when the CE is calculated using the measured SI. Indeed, shorter aggregation intervals yield a larger improvement of the correction when using the measured SI rather than temperature, as demonstrated by larger values of the difference $\Delta\text{RMSE} = \text{RMSE}[\text{CE}(U_w, T)] - \text{RMSE}[\text{CE}(U_w, \text{SI})]$.

The fact that the amount of scatter reduction ΔRMSE increases with shorter aggregation intervals, seems to support the need of high-resolution measurements to improve the accuracy of the snow data. For instance, the scatter resulting from the correction of 30-min accumulation measurements based on wind speed and temperature can be achieved for 10-min accumulation measurements if the SI is used for the correction. Thus, by using the SI in the transfer function instead of temperature, one can either achieve a higher skill for a given aggregation time or achieve a higher aggregation interval with a RMSE similar to the one traditionally obtained for a longer aggregation interval.

5. CFD simulation and validation

The following section presents the CFD modeling framework used to compare to the observations in section 3 and to validate the physical basis of using the SI as an explanatory variable for the CE.

a. *Airflow modeling and CE calculation*

The flow field around a SA shielded gauge was numerically simulated using the Open Foam software and is described by Colli et al. (2015). The time-averaged air velocity, turbulent kinetic energy and pressure fields were solved by means of a Reynolds averaged Navier–Stokes k–ω SST model.

The trajectories of dry snow particles falling through the CFD flow field are calculated using a Lagrangian model (Colli et al. 2015) for wind speeds between 1 and 8 m s^{-1}. The particle characteristics are from Rasmussen et al. (1999).

Several particle sizes were simulated to capture the dependence of CE on particle size. The PSD of snowfall events can be described using the gamma distribution,

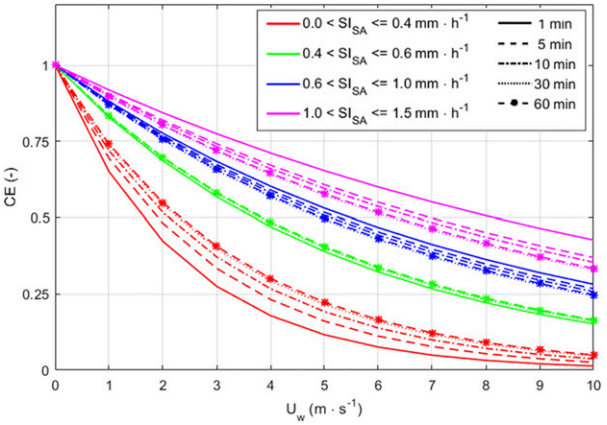

FIG. 8. Best-fit CE(U_w, SI) curves of the SA shielded snow gauge at the Marshall Field Site at 1, 5, 10, 30, and 60-min sampling intervals (different line types) grouped by the measured SI (different line colors).

TABLE 4. RMSE of precipitation measurements made by the SA shielded gauge at the Marshall Field Site over different aggregation intervals Δt after applying the correction based on SI, CE(U_w, SI_{SA}), and air temperature, CE(U_w, T), and their difference ΔRMSE.

Δt (min)	RMSE [CE(U_w, T)] (—)	RMSE [CE(U_w, SI_{SA})] (—)	ΔRMSE (—)
1	0.26	0.16	0.10
5	0.19	0.12	0.07
10	0.16	0.11	0.05
30	0.13	0.08	0.04
60	0.12	0.07	0.05

as shown by Brandes et al. (2007), which is similar to the one by Marshall and Palmer (1948), but uses a shape parameter:

$$N(D) = N_0 \times D^{\mu} \times e^{-\lambda \times D}, \tag{6}$$

where D is the snowflake diameter, N_0 is the scale parameter, μ characterizes the curvature, and λ is the slope of the distribution. According to Brandes et al. (2007) μ can be estimated by the following expression: $\mu = -0.00499\lambda^2 + 0.798\lambda - 0.666$. In this work we adopted a general intercept value equal to $N_0 = 10^6\,\mathrm{mm}^{-1-\mu}\,\mathrm{m}^{-3}$ and, based on observations, the slope parameters used are $0.5 < \lambda < 1.5\,\mathrm{mm}^{-1}$ (Brandes et al. 2007; Houze et al. 1979). The estimation of CE is based on the particle counting technique described in Colli et al. (2016b):

$$\mathrm{CE}(U_w) = \frac{\int_0^{d_{p\max}} V_w(d_p) A_{\mathrm{inside}}(d_p, U_w) N(d_p) d_p}{\int_0^{d_{p\max}} V_w(d_p) A_{\mathrm{gauge}}(d_p, U_w) N(d_p) d_p}, \tag{7}$$

where $A_{\mathrm{inside}}(d_p, U_w)$ is the effective collecting area associated with the number of particles collected by the gauge and $A_{\mathrm{gauge}}(d_p, U_w)$ is the area associated with the entering particles in the case of undisturbed airflow. Finally, $V_w(d_p)$ is the equivalent water volume.

b. PSD and snowfall intensity collected by the gauge

The link between snowfall intensity computed based on the simulation and the slope of the size distribution is given in Table 5. It shows that steeper slopes of the PSD (represented by higher λ), and as a consequence smaller mean particle sizes, are characterized by lower values of the CE. This is due to the fact that the trajectories of the smaller particles can be easily deflected by the airflow around the gauge collector. Furthermore, the simulation results (Table 5) show that CE becomes sensitive to the snow particle distribution (here reported by the λ term) when the wind speed is higher than $3\,\mathrm{m\,s^{-1}}$.

TABLE 5. Ratio between the collected SI and the reference SI by varying the wind speed U_w ($\mathrm{m\,s^{-1}}$) and the slope parameter λ ($\mathrm{mm^{-1}}$) of the PSD.

λ	0.5	0.7	0.9	1.1	1.3	1.5	1.7	1.9
SI	8.49	3.86	2.1	1.26	0.81	0.54	0.38	0.27
$U_w = 1\,\mathrm{m\,s^{-1}}$	1	1	1	1	1	1	1	1
$U_w = 2\,\mathrm{m\,s^{-1}}$	0.97	0.97	0.97	0.97	0.97	0.97	0.97	0.97
$U_w = 3\,\mathrm{m\,s^{-1}}$	0.94	0.93	0.93	0.93	0.93	0.93	0.93	0.92
$U_w = 4\,\mathrm{m\,s^{-1}}$	0.87	0.86	0.85	0.84	0.84	0.83	0.82	0.81
$U_w = 5\,\mathrm{m\,s^{-1}}$	0.78	0.74	0.7	0.67	0.63	0.6	0.57	0.54
$U_w = 6\,\mathrm{m\,s^{-1}}$	0.69	0.61	0.54	0.47	0.41	0.35	0.31	0.27
$U_w = 7\,\mathrm{m\,s^{-1}}$	0.51	0.39	0.29	0.21	0.15	0.11	0.08	0.06
$U_w = 8\,\mathrm{m\,s^{-1}}$	0.32	0.19	0.11	0.06	0.03	0.02	0.01	0.01

The CFD analysis performed by Thériault et al. (2012) found that the type of precipitation and their sizes explained some of the scatter in the gauge catch efficiency for a given U_w. Colli et al. (2015) confirmed this conclusion by providing different CE(U_w) functions as well as an improved drag coefficient using the same slope parameters (λ = 0.25, 0.50, and $1\,\mathrm{mm^{-1}}$) as in Thériault et al. (2012).

To link the snowfall intensity with the PSD, an example of the simulated size distribution of dry snow particles that fall into the gauge is shown in Fig. 9 for a sample precipitation characterized by $\lambda = 1.0\,\mathrm{mm^{-1}}$ and $N_0 = 10^6\,\mathrm{mm}^{-1-\mu}\,\mathrm{m}^{-3}$. These PSD parameters were suggested by Houze et al. (1979) who observed the snow size distribution in different atmospheric conditions. In agreement with Fig. 9 of Thériault et al. (2012), it is shown that the gauge starts missing the lower particle sizes when U_w approaches $4\,\mathrm{m\,s^{-1}}$, and higher wind speeds correspond to narrower ranges of particle diameters that

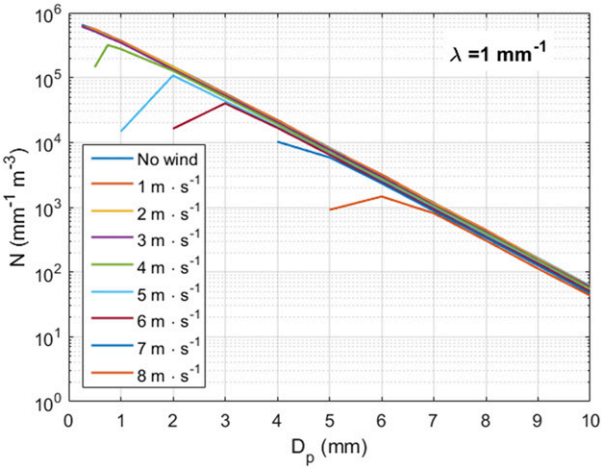

FIG. 9. CFD simulated PSD of dry snow collected by the SA shielded gauge under different wind conditions using $\lambda = 1.0\,\mathrm{mm^{-1}}$ and $N_0 = 10^6\,\mathrm{mm}^{-1-\mu}\,\mathrm{m}^{-3}$.

are collected by the gauge (and higher curvature parameter μ). A lower number of such smaller particles fall in the gauge at $4\,\mathrm{m\,s^{-1}}$ than previously found by Thériault et al. (2012). This is probably due to the updated drag coefficient.

For larger diameters, the PSD of the precipitation collected by the gauge maintains the same slope λ of the reference and slightly decreases the concentration number N_0 with increasing U_w. The collected $N(D_p)$ values are lower than the reference PSD but maintain the same order of magnitude. An exception is represented by the smaller diameter of the PSDs collected under wind speeds higher than $4\,\mathrm{m\,s^{-1}}$. In this case, the $N(D_p)$ value is approximately one order of magnitude lower than the reference one. The wind-induced underestimation of the $\mathrm{SI_{SA}}$ for a given λ is due to the massive loss of the many small particles, which fail to fall into the gauge.

c. *Comparing the results of field observations and CFD simulations*

The computed CE variation with wind speed as a function of SI is shown in Fig. 10. The results of the CFD trajectory analysis are shown in Fig. 10a while the Marshall Field Site measurements are reported in Fig. 10b. The plot is comparable to Fig. 8 of Colli et al. (2015) where the correlation between the simulated CE and the PSD was discussed. For any given wind speed, a set of eight CE values have been computed according to the slope λ of the reference PSD, which is correlated with the SI measured by the gauge, Eq. (3).

The CFD results show that when the wind speed is higher than $3\,\mathrm{m\,s^{-1}}$, there is an abrupt increase of the CE scatter from $1 < \mathrm{SI_{SA}} < 1.5\,\mathrm{mm\,h^{-1}}$ (red points) to $0 < \mathrm{SI_{SA}} < 0.5\,\mathrm{mm\,h^{-1}}$ (blue points), associated with a decrease of the CE at any given wind speed (Fig. 10a). When the average wind speed is lower or equal to $3\,\mathrm{m\,s^{-1}}$ the dependency of the CE on the measured SI becomes less significant, meaning that even the smaller particles are mostly collected by the SA shielded gauge. The latter result is not confirmed by the field measurements provided in Fig. 1 that show a persistent scattering of the CE even at the lower wind speeds. Such behavior has been already explained by Colli et al. (2016b) that demonstrated the role of the airflow turbulence generated by the wind shield in the CE scattering by means of time-dependent CFD simulation.

The results of the CFD simulations therefore highlight the physical dependency between the CE and the SI measured by the gauge, and this dependency varies according to the wind speed. Figure 10b shows the CE field observations for the 10-min aggregation interval dataset, categorized by SI confirming the dependency between collected precipitation, measured intensity and wind speed.

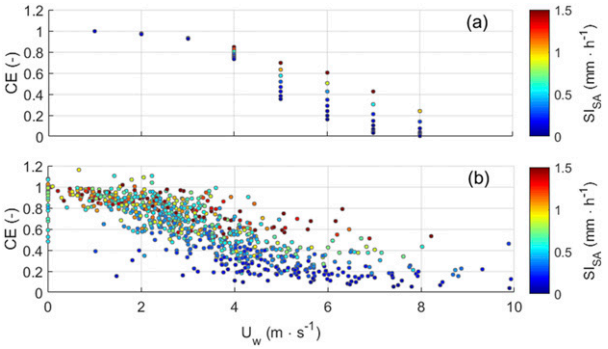

FIG. 10. CE scatter of the 10-min SA shielded gauge measurements simulated by means of the (a) time-averaged CFD model and (b) field measurements made at the Marshall Field Site. Data are color coded according to the measured SI.

The added value of using the SI in the transfer function is best visualized in the $\mathrm{SI_{SA}}$ versus $\mathrm{SI_{REF}}$ scatterplot shown in Fig. 11a, where $\mathrm{SI_{REF}}$ is the reference SI (assumed coincident with $\mathrm{SI_{DFIR}}$ for the field data). In this graph, where the wind speed is color-coded according to the side bar, the iso-CE lines would be linear (gray dotted lines) in the absence of a clear influence of the $\mathrm{SI_{SA}}$ on the CE. A clear deviation from linearity is observed, showing that the collection efficiency increases far beyond linearity with the measured SI at any wind speed class. This deviation vanishes when $U_w \to 0$ and increases with the wind speed, therefore justifying the larger spread of CE values observed toward the right-hand side of Figs. 10a and 10b.

6. Concluding remarks

The present analysis of recent WMO-SPICE quality controlled 30-min accumulation data from the Marshall Field Site (Colorado) revealed that the wind-induced undercatch of solid precipitation gauges is best correlated with the measured snowfall intensity, rather than temperature, in addition to wind speed. While the environmental temperature provides general relevant information about whether the precipitation is rain (Auer 1974; Sims and Liu 2015), wet or dry snow (Rasmussen et al. 1999; Sims and Liu 2015) it is not clear how the exact type of solid precipitation can be easily determined in the field. At cold temperatures, which are often associated with dry snow, it is also possible to observe rime particles that would have higher collection efficiency (Thériault et al. 2012). On the other hand, the measured snowfall intensity has the advantage of including information about the PSD (Pruppacher and Klett 2010). Optimal curve fitting used to derive the

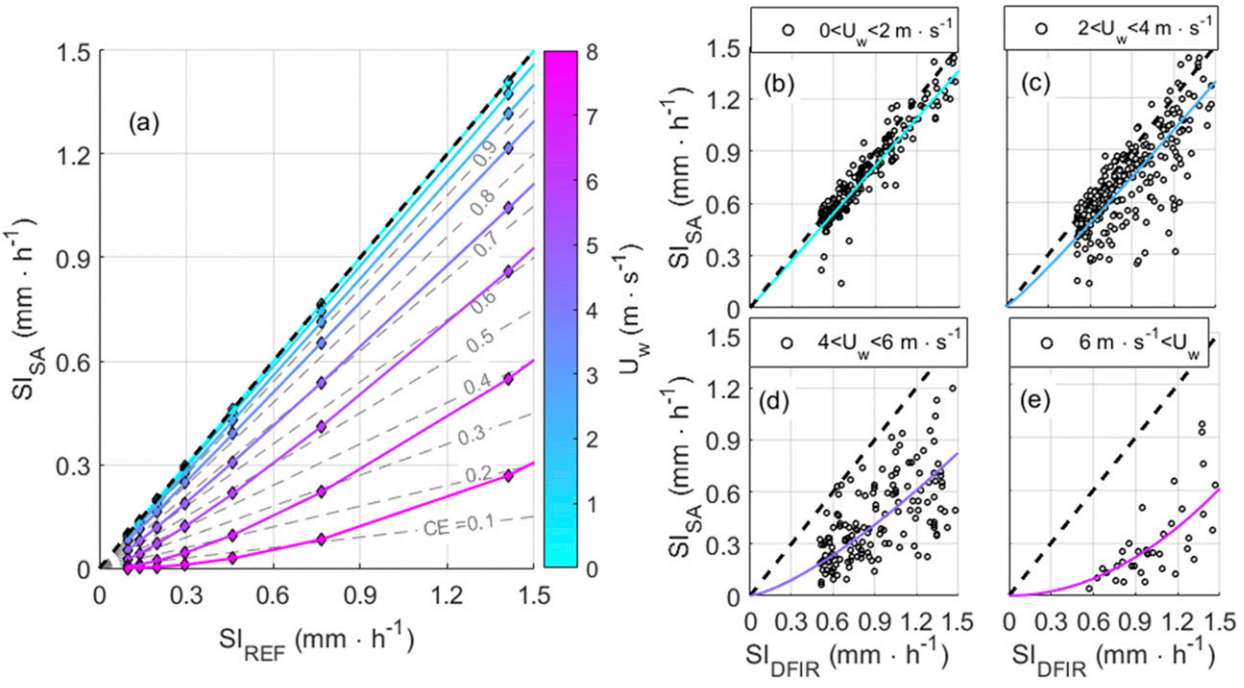

FIG. 11. (a) Deviation from linearity of the CE (gray dotted lines) when increasing the wind speed (color coded according to the side bar) in the measured vs reference SI plane. The deviation is evident in both the results of the (a) numerical simulation (solid colored lines and diamonds) and (b)–(e) field data (white circles in panels) although with some residual scatter. The field data are presented together with power law regressions performed for various wind speed classes.

transfer function for the GEONOR gauge in a Single Alter shield and in a DFIR configuration indicates that accounting for SI indeed reduces the scatter of the residuals.

This result is confirmed by the analysis of data from other field sites, such as CARE (Canada) and Haukeliseter (Norway), and shows a consistent behavior under different climatological conditions. Recent results from Chubb et al. (2015) found improved undercatch correction after including the precipitation amount parameter in the catch ratio curves for an ETI weighing gauge using data collected in the Snowy Mountains of Australia. This supports our results and suggests that other snow gauges can benefit from this type of adjustment.

The physical basis for the improved parameterization of the transfer function by using the measured SI was shown through CFD modeling of the gauge snow collection process to be due to the correlation of large particles with high intensities. Large particles are preferentially collected by a snow gauge, even in strong wind, due to their higher fall velocity, allowing them to break through streamlines of flow above the gauge and be collected. The CFD modeling was able to reproduce the CE pattern observed in the field providing strong evidence of the hypothesized behavior.

The analysis of the optimal aggregation interval of snowfall measurements was based on the evaluation of the residual data scattering after applying adjustments based on wind speed and either environmental temperature or the measured SI. It has been observed that shorter accumulation intervals increase the dependency of the CE on SI and a stronger benefit in using the proposed approach. On the other hand, it was also observed that larger accumulation intervals are generally associated with a smaller residual scattering of the measurements. According to our analysis, the 10-min aggregation interval may represent a trade-off point between the availability of correlated SI and CE observations and the need of accumulating significant amounts of snowfall when lower precipitation intensities occur.

Overall, these findings provide an attractive method to improve operational measurements since no additional instrument, except for a wind sensor, is required to derive the adjusted estimates of snow accumulation.

Acknowledgments. J. M. Thériault was funded by the Natural Sciences and Engineering Research Council (NSERC) of Canada and Canadian Research Chair Tier 2.

Data availability statement. In this paper, the WMO-SPICE 30-min quality controlled site event datasets (SEDS)

used for this work are available in the online supplement material.

REFERENCES

Alter, J. C., 1937: Shielded storage precipitation gages. *Mon. Wea. Rev.*, **65**, 262–265, https://doi.org/10.1175/1520-0493(1937)65<262:SSPG>2.0.CO;2.

Auer, A. H., 1974: The rain versus snow threshold temperature. *Weatherwise*, **27**, 67, https://doi.org/10.1080/00431672.1974.9931684.

Brandes, E. A., K. Ikeda, G. Zhang, M. Schönhuber, and R. M. Rasmussen, 2007: A statistical and physical description of hydrometeor distributions in Colorado snowstorms using a video disdrometer. *J. Appl. Meteor. Climatol.*, **46**, 634–650, https://doi.org/10.1175/JAM2489.1.

Chubb, T., M. J. Manton, S. T. Siems, A. D. Peace, and S. P. Bilish, 2015: Estimation of wind-induced losses from a precipitation gauge network in the Australian snowy mountains. *J. Hydrometeor.*, **16**, 2619–2638, https://doi.org/10.1175/JHM-D-14-0216.1.

Colli, M., R. Rasmussen, J. M. Thériault, L. G. Lanza, C. B. Baker, and J. Kochendorfer, 2015: An improved trajectory model to evaluate the collection performance of snow gauges. *J. Appl. Meteor. Climatol.*, **54**, 1826–1836, https://doi.org/10.1175/JAMC-D-15-0035.1.

——, L. G. Lanza, R. M. Rasmussen, and J. M. Thériault, 2016a: The collection efficiency of shielded and unshielded precipitation gauges. Part I: CFD airflow modelling. *J. Hydrometeor.*, **17**, 231–243, https://doi.org/10.1175/JHM-D-15-0010.1.

——, ——, ——, and ——, 2016b: The collection efficiency of shielded and unshielded precipitation gauges. Part II: Modelling particle trajectories. *J. Hydrometeor.*, **17**, 245–255, https://doi.org/10.1175/JHM-D-15-0011.1.

Constantinescu, S., W. F. Krajewski, C. E. Ozdemir, and T. Tokyay, 2007: Simulation of flow around raingauges: Comparison of LES with RANS models. *J. Adv. Water Resour.*, **30**, 43–58, https://doi.org/10.1016/j.advwatres.2006.02.011.

Eldred, M. S., H. Agarwal, V. M. Perez, S. F. Jr. Wojtkiewicz, and J. E. Renaud, 2007: Investigation of reliability method formulations in DAKOTA/UQ. *Struct. Infrastruct. Eng.*, **3**, 199–213, https://doi.org/10.1080/15732470500254618.

Folland, C. K., 1988: Numerical models of the raingauge exposure problem, field experiments and an improved collector design. *Quart. J. Roy. Meteor. Soc.*, **114**, 1485–1516, https://doi.org/10.1002/qj.49711448407.

Gergely, M., and T. J. Garrett, 2016: Impact of the natural variability in snowflake diameter, aspect ratio, and orientation on modeled snowfall radar reflectivity. *J. Geophys. Res. Atmos.*, **121**, 12 236–12 252, https://doi.org/10.1002/2016JD025192.

Goodison, B., P. Louie, and D. Yang, 1998: WMO solid precipitation measurement intercomparison: Final report. WMO Tech. Doc. 872, World Meteorological Organization, 212 pp., https://globalcryospherewatch.org/bestpractices/docs/WMOtd872.pdf.

Houze, R. A., P. V. Hobbs, and P. H. Herzegh, 1979: Size distributions of precipitation particles in frontal clouds. *J. Atmos. Sci.*, **36**, 156–162, https://doi.org/10.1175/1520-0469(1979)036<0156:SDOPPI>2.0.CO;2.

Kochendorfer, J., and Coauthors, 2017a: The quantification and correction of wind-induced precipitation measurement errors. *Hydrol. Earth Syst. Sci.*, **21**, 1973–1989, https://doi.org/10.5194/hess-21-1973-2017.

——, and Coauthors, 2017b: Analysis of single-Alter-shielded and unshielded measurements of mixed and solid precipitation from WMO-SPICE. *Hydrol. Earth Syst. Sci.*, **21**, 3525–3542, https://doi.org/10.5194/hess-21-3525-2017.

——, and Coauthors, 2018: Testing and development of transfer functions for weighing precipitation gauges in WMO-SPICE. *Hydrol. Earth Syst. Sci.*, **22**, 1437–1452, https://doi.org/10.5194/hess-22-1437-2018.

Marshall, J. S., and W. M. Palmer, 1948: The distribution of raindrops with size. *J. Meteor.*, **5**, 165–166, https://doi.org/10.1175/1520-0469(1948)005<0165:TDORWS>2.0.CO;2.

Matrosov, S. Y., C. Campbell, D. Kingsmill, and E. Sukovich, 2009: Assessing snowfall rates from X-band radar reflectivity measurements. *J. Atmos. Oceanic Technol.*, **26**, 2324–2339, https://doi.org/10.1175/2009JTECHA1238.1.

Nešpor, V., and B. Sevruk, 1999: Estimation of wind-induced error of rainfall gauge measurements using a numerical simulation. *J. Atmos. Oceanic Technol.*, **16**, 450–464, https://doi.org/10.1175/1520-0426(1999)016<0450:EOWIEO>2.0.CO;2.

Nitu, R., and Coauthors, 2018: WMO Solid Precipitation Intercomparison Experiment (SPICE) (2012–2015). Instruments and Observing Methods Rep. No. 131, 1445 pp., https://library.wmo.int/doc_num.php?explnum_id=5686.

Pruppacher, H. R., and J. D. Klett, 2010: *Microphysics of Clouds and Precipitation, Atmospheric and Oceanographic Sciences Library*. Springer, 954 pp.

Rasmussen, R. M., J. Vivekanandan, J. Cole, B. Myers, and C. Masters, 1999: The estimation of snowfall rate using visibility. *J. Appl. Meteor.*, **38**, 1542–1563, https://doi.org/10.1175/1520-0450(1999)038<1542:TEOSRU>2.0.CO;2.

——, and Coauthors, 2012: How well are we measuring snow: The NOAA/FAA/NCAR winter precipitation test bed. *Bull. Amer. Meteor. Soc.*, **93**, 811–829, https://doi.org/10.1175/BAMS-D-11-00052.1.

Reverdin, A., 2016: Description of the quality control and event selection procedures used within the WMO-SPICE project. Tech. Doc., 11 pp., https://www.wmo.int/pages/prog/www/IMOP/publications/IOM-125_TECO_2016/Session_3/P3(10)_Reverdin.pdf.

Sims, E. M., and G. Liu, 2015: A parameterization of the probability of snow–rain transition. *J. Hydrometeor.*, **16**, 1466–1477, https://doi.org/10.1175/JHM-D-14-0211.1.

Thériault, J., R. Rasmussen, K. Ikeda, and S. Landolt, 2012: Dependence of snow gauge collection efficiency on snowflake characteristics. *J. Appl. Meteor. Climatol.*, **51**, 745–762, https://doi.org/10.1175/JAMC-D-11-0116.1.

——, ——, E. Petro, J. Trépanier, M. Colli, and L. G. Lanza, 2015: Impact of wind direction, wind speed, and particle characteristics on the collection efficiency of the double fence intercomparison reference. *J. Appl. Meteor. Climatol.*, **54**, 1918–1930, https://doi.org/10.1175/JAMC-D-15-0034.1.

Thom, A. S., 1975: Momentum, mass and heat exchange of plant communities. *Vegetation and the Atmosphere*, Vol. 1, J. L. Monteith, Ed., Academic Press, 57–110.

WMO, 2014: Guide to meteorological instruments and methods of observation. 8th ed. WMO 8, 1139 pp., http://www.wmo.int/pages/prog/www/IMOP/CIMO-Guide.html.

Wolff, M. A., K. Isaksen, A. Petersen-Øverleir, K. Ødemark, T. Reitan, and R. Bækkan, 2015: Derivation of a new continuous adjustment function for correcting wind-induced loss of solid precipitation: Results of a Norwegian field study. *Hydrol. Earth Syst. Sci.*, **9**, 10 043–10 084, https://doi.org/10.5194/hessd-11-10043-2014.

Yang, D., and Coauthors, 1999: Quantification of precipitation measurement discontinuity induced by wind shields on national gauges. *Water Resour. Res.*, **35**, 491–508, https://doi.org/10.1029/1998WR900042.